Physical Model of Contractile Ring Initiation in Dividing Cells

Roie Shlomovitz and Nir S. Gov
Chemical Physics, The Weizmann Institute of Science, Rehovot, Israel

ABSTRACT We present a physical mechanism to describe initiation of the contractile ring during cell division. The model couples the membrane curvature with the contractile forces produced by protein clusters attached to the membrane. These protein clusters are mobile on the membrane and possess either an isotropic or an anisotropic spontaneous curvature. Our results show that under these conditions the contraction force gives rise to an instability that corresponds in a closed cellular system to the initiation of the contractile ring. We find a quantization of this process at distinct length-scales, which we compare to available data for different types of eukaryote cells.

INTRODUCTION

The phenomenon of cell division is one of the most central tenets of living cells (1,2). The process of physical division itself is driven by the formation of the contractile ring (CR) on the cell membrane, which then proceeds to shrink, dragging the membrane with it (3), or organizes the formation of a septum that divides the cell (4). The main protein content of this ring in eukaryotes is actin filaments and myosin motors, which cluster on the membrane and produce a contractile force. Many other proteins reside in the ring and contribute to actin filament assembly, bundling, dynamics, and membrane association. Recent findings have revealed that some of these additional proteins in the ring may have the propensity to directly alter the composition and/or curvature of the plasma membrane (5–9).

We propose in this work that the initiation of the CR is through a mechanism of mechanical dynamic instability occurring on the cell membrane. The cell has control over the position and timing in which the conditions of this mechanical instability occur, through various types of cell-cycle machinery. This is a relatively simple model that couples the membrane elasticity to the contractile forces produced by an underlying cytoskeletal network, through the introduction of freely diffusing membrane proteins that nucleate the formation of this contractile network (CN) (Fig. 1, *b* and *c*), and possess a spontaneous curvature. We use here cylindrical geometry to describe the dynamics relevant to the process of cell division. We show that when the conditions are right such a model displays a dynamical instability that can explain the mechanism for the aggregation of the CN into a CR.

Previously (10) we showed that such a simple model can already give rise to several observed membrane shapes, depending on the spontaneous curvature of the membrane proteins that couple the cytoskeleton with the membrane. In this work, we extend the previous model (10) to include the effect of contractile forces and cylindrical geometry.

The important role played by membrane curvature in determining the membrane composition was recently demonstrated (11), even with very mild curvatures (12). A spontaneous curvature of membrane proteins and clusters can arise from the geometrical shape of the membrane-bound aggregate (13), and through interactions with the membrane components that change the local concentrations of different proteins and lipids. Specifically, it was found that the membrane at the furrow develops a unique composition of lipids and proteins that is very different between the inner and outer leaflets (5–9), a property that is known to produce spontaneous curvature. Several theoretical studies have shown that a membrane with components that have a spontaneous curvature, and no active forces, can become unstable and go through dramatic shape changes and phase separation (14,15).

In this work we deal with three possible cases of CN spontaneous curvature that will lead to furrowlike instability on a cylinder; 1), a CN with an isotropic concave spontaneous curvature; 2), an anisotropic convex curvature; and 3), an anisotropic concave curvature (Fig. 1 *a*). The first case has its curvature energy minimized on the inner surface of spherical invaginations that protrude into the cell (as in caveolae). Such a CN will therefore prefer the region of a furrow to the flat parts of a cylinder, assuming that the cylinder radius is not too small (Fig. 1, *a* and *b*). The second and third cases describe linear complexes in the shape of arcs and rings. If these have a convex spontaneous curvature (case 2) with a radius of curvature that is smaller than the radius of the cylinder, then they will naturally prefer to aggregate at the narrower furrow (and at the hemispherical poles) since they are aligned in the azimuthal direction (14) (Fig. 1, *a* and *c*). The third case has concave spontaneous curvature, so that these complexes aggregate in the furrow when they are aligned along the axial direction (Fig. 1 *a*). We are motivated to consider linear, arclike structures since these turn out to be the shapes of many membrane proteins that can produce

Submitted April 23, 2007, and accepted for publication September 17, 2007.

Address reprint requests to Roie Shlomovitz, Tel.: 972-934-6031; E-mail: roie@wisemail.weizmann.ac.il.

Editor: Michael Edidin.

0006-3495/08/02/1155/14 $2.00

doi: 10.1529/biophysj.107.111351

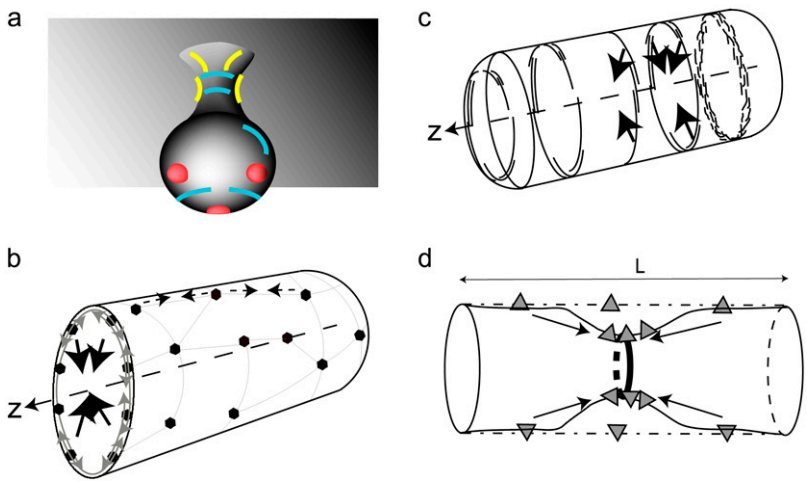

FIGURE 1 (*a*) Different spontaneous curvatures of membranal clusters: concave isotropic (*red caps*), convex-anisotropic (*light-blue arcs*), and concave-anisotropic (*yellow arcs*). The figure shows a small membrane invagination that protrudes into the cell, and is therefore a surface where isotropic-concave proteins (*red caps*) aggregate. Note that the arcs shown do not represent single CN proteins, but an aggregate of many such elements. (*b*) Membrane aggregates of myosin (and other proteins), connected by actin filaments. The myosin contractility creates forces in the axial direction (*dashed arrows*) which tend to condense the ring, and forces in the azimuthal direction (*shaded arrows*) that result in a radial contraction (*large arrows*). (*c*) Filaments (and other host proteins), which contract and create a radial contractile force. (*d*) A schematic picture of the instability that drives the initiation of the CR. The dash-dot line corresponds to the initial uniform system ($h = 0$, $n = n_0$), and the triangles represent the mobile CN elements.

curvature (16), while an isotropic spontaneous curvature may arise from a cluster of such proteins.

The instability (aggregation) in our model is not driven, however, by spontaneous curvature alone (in contrast with (17)), which is also known to give rise to pearling-instability (18). Such phase separation occurs at thermodynamic equilibrium, while our model involves active forces that cannot be described in these equilibrium terms. It is the combination of spontaneous curvature and contractile forces that drives the instability in our model, and is the unique feature of this mechanism. We find that the appearance of instability depends on the length of the cylindrical membrane, its radius, surface tension and the strength of the contractility. Control of these parameters allows the cell to direct the initiation of the CR spatially and temporally. Some of these parameters may be varied experimentally and used to test the validity of our model.

Other models that introduced membrane dynamic instability in the cytokinesis process, were previously proposed over the years (19–24). These models assumed a uniform contractile layer at the membrane, which is destabilized when division is needed, by weakening the contraction at the cell poles. This leads to uniform and cell-wide contraction of this layer toward the cell equator, forming a ring which then proceeds to shrink and divide the cell. These models are different from ours in many aspects; first, they assume already the existence of a contractile layer which has a density gradient such that it is maximal at the equator. It is the initiation of such a band during the telophase that we propose to explain. Furthermore, such a uniform contractile layer does not seem to cover the whole cell in some cases, but rather form directly at the cell equator before division (25). Another model for ring formation that does not include any membrane deformations and radial contraction, our key components, was proposed recently (26). Note that by limiting ourselves to the limit of small deformations our model can be written in terms of linear equations and solved analytically. We therefore model the process of initiation of the CR, while we do not describe the latter stages of cytokinesis (27,28), which require larger forces, large-scale motion, and internal rearrangement.

To summarize, we introduce a new model that couples, for the first time to our knowledge, the membrane curvature and the contractile forces of the cytoskeleton. This model produces a dynamic instability that in the context of cytokinesis may provide a mechanism for the initiation of the CR in dividing cells. In the next sections, we first introduce and solve the model, and then discuss the results. We compare the results of our model to the observations of CR initiation in eukaryotes in Comparison to Experimental Observations. The conclusion and a summary of our main experimental predictions are given in the final sections.

MODEL

The general form of a CN that we consider is shown schematically in Fig. 1 *b*. There are membranal clusters of proteins (containing myosin motors) that are connected by bundles of actin filaments, thus creating a CN bound to the membrane (2,25,29,30) (Fig. 1 *b*). The contractile forces in this network are in the plane of the membrane, and result in two effects:

1. The forces in the azimuthal direction (Fig. 1 *b*, *shaded arrows*) give rise, due to the cylindrical symmetry, to contraction in the radial direction (Fig. 1 *b*, *large arrows*). We assume here that we are dealing with small fluctuations around a uniform distribution, such that the contractile force is taken to be linearly proportional to the local deviation in the density of the CN $n(z)$, i.e., $F_r \propto n(z)$.
2. Forces in the axial z-direction (Fig. 1 *b*, *dashed arrows*) balance each other, unless there are gradients in the density of the CN, so we get $F_z \propto \nabla n(z)$. Due to the assumed rotational invariance, we limit ourselves to closed rings.

Our theoretical description follows the works of Manneville et al. (31) and Ramaswamy et al. (32) on active membranes.

The most crucial property beyond the production of forces is the spontaneous curvature of the membranal CN, which may couple either to the local mean curvature of the membrane (isotropic case) or to only one of the principal curvatures (anisotropic case). We will treat both cases below, where $\bar{H}$ represents the spontaneous curvature of the CN. For concave spontaneous curvature we have $\bar{H} > 0$, and for convex curvature $\bar{H} < 0$.

The bending energy of a membrane, with effective bending modulus κ and spontaneous curvature R, is

$$\mathcal{E}_b = \int \left[\frac{1}{2}\kappa \left(H + \frac{1}{2R} \right)^2 - \kappa H_p \bar{H} \frac{n(z)}{n_0} \right] d^2 r, \qquad (1)$$

where H_p is the principal curvature that couples with the spontaneous curvature of the CN (see below), and H is the mean curvature of the membrane (33) (expanded to first-order in h),

$$H = \frac{r(z)r''(z) - r'(z)^2 - 1}{2r(z)(1 + r'(z)^2)^{3/2}} = \frac{1}{2}\left(h''(z) - \frac{1}{R} + \frac{h(z)}{R^2} \right), \qquad (2)$$

where $r(z)$ is the radius of the surface, and $h(z)$ is a small deviation: $r(z) = R + h(z)$, where R is the spontaneous radius of the cylindrical membrane, including the effect of a uniform distribution n_0 of CN. The first term in Eq. 1 describes the Helfrich Hamiltonian of a membrane with spontaneous curvature R.

The second term in Eq. 1 describes the coupling of the CN with a spontaneous curvature $\bar{H}n(z)/n_0$ to the membrane, where $n(z)$ denotes small deviations in the concentration from the uniform distribution n_0. (The term in (31) that contains $n(z)^2$ simply modifies the diffusion coefficient of the CN proteins by a constant term. We assume here that the measured diffusion coefficient of these elements already has this effect included.) For a concave isotropic CN, the coupling is to the mean curvature of the membrane, and $H_p = H$. For the flat membrane ($R \to \infty$), we recover the expressions that appear in Manneville et al. (31). (We assume that $n_0 \ll n_{sat}$, where n_{sat} is the saturation density of the CN complexes. The spontaneous curvature of the CN alone is given by $\bar{H}_{sat} = \bar{H} n_{sat}/n_o$, and $R > 1/\bar{H}_{sat}$, i.e., that, due to bending energy, the CNs prefer a smaller radius of the cylindrical membrane. If $R < 1/\bar{H}_{sat}$, the CNs prefer a larger radius, and no contractile instability occurs.)

For the anisotropic CNs, the proteins couple only to one of the principle curvatures of the membrane. We will assume here that the CN elements have a fixed orientation in the plane of the membrane, such that they minimize their bending energy on a cylindrical membrane. This means that for the convex-anisotropic case the CN will align in the azimuthal direction (Fig. 1, *a–c*), and couple only to the local changes in the radius $r(z)$, i.e., $H_p = h(z)/R^2$ (Eq. 1). For the concave-anisotropic case the CN elements are aligned along the axis of the cylinder (Fig. 1 *a*), so they couple only to the local variations in the radius along the axial direction, i.e., $H_p = h''(z)$ (Eq. 1).

The surface tension energy of the membrane is

$$\mathcal{E}_s = \frac{1}{2}\sigma \int \left(\frac{h}{R} + h''(z)^2 \right) R dz d\theta + O(h^2), \qquad (3)$$

where σ is the surface tension coefficient. We will assume that the linear term in h is balanced, e.g., by osmotic pressure difference, such that a cylinder with radius R is the equilibrium shape for a uniform distribution of CN. Alternatively, the radius of the uniform system may be stabilized by coupling the membrane to a rigid shell, as happens in yeast.

The equation of motion for the membrane height deflection along the cylinder axis, $h(z)$, is given by (10)

$$\begin{aligned} \frac{\partial h(z)}{\partial t} &= \int \mathcal{O}(r - r') \left(-\frac{\delta F}{\delta h(r')} - A\, n(r') \right) d^2 r' \\ &= -\hat{\mathcal{O}} \left(\kappa \nabla^4 h + \nabla^2 h \left(\frac{\kappa}{R^2} - \sigma \right) + \kappa \frac{h}{R^4} \right) \\ &\quad + \hat{\mathcal{O}} \left(\frac{\kappa \bar{H}}{n_0} \nabla^2 n + n \left(\frac{\bar{H}\kappa}{n_0 R^2} - A \right) \right), \end{aligned} \qquad (4)$$

where $F = \mathcal{E}_b + \mathcal{E}_s$ is the total free energy of the membrane with the freely diffusing network (31,32), $A > 0$ is the proportionality constant which relates the local CN density $n(r')$ with the resulting contractile force, and $\mathcal{O}(r - r')$ is the Oseen-tensor describing the viscous drag of the fluid surrounding the membrane. We assume that the uniform system is stable, so that only deviations from uniformity give rise to finite membrane forces, and we keep these deviations to first order in Eq. 4. The stability of the uniform system is corroborated below, where $\omega' \to 0$ for $q \to 0$. For restricted fluid flows, the local integration over the Oseen tensor gives a constant factor of $\hat{\mathcal{O}} = d/4\eta$, where d is the length scale of the fluid confinement. This scale may be dictated by the density of the CN below the membrane.

The equation for the local density $n(z)$ is given by a conservation equation

$$\begin{aligned} \frac{\partial n(z)}{\partial t} &= D\nabla^2 n(z) + \Lambda n_0 \nabla^2 \frac{\delta F}{\delta n} = (D - D^*)\nabla^2 n(z) \\ &\quad - \kappa \bar{H} \Lambda \left(\nabla^4 h + \frac{\nabla^2 h}{R^2} \right), \end{aligned} \qquad (5)$$

where D is the in-membrane diffusion coefficient and Λ is the mobility of the CN aggregates.

The term D^* is the effective result of the contractile forces that act inside the plane of the membrane, i.e., along the cylinder axis (Fig. 1 *b*). They therefore do not contribute to the contractile forces, since in the linear regime they only modify the effective diffusion coefficient of the CN elements (27). If this in-plane contractility is dominant, the effective diffusion coefficient is negative, and the CN is unstable at all

wavelengths. The instability then becomes trivial and independent on any membrane parameters, such as tension and length. The shortest wavelengths of such a system are the most unstable, which would result in the formation of numerous CRs throughout the CN band. This is not observed, so we therefore keep the effective diffusion coefficient $D - D^*$ positive. From here onwards, D represents this positive overall effective diffusion coefficient.

For an infinitely long cylinder, we Fourier-transform Eqs. 4 and 5 for the isotropic case

$$\begin{pmatrix} \dot{h} \\ \dot{n} \end{pmatrix} = \begin{pmatrix} -\hat{\mathcal{O}}(\kappa q^4 + (\sigma - \kappa/R^2)q^2 + \kappa/R^4) & \hat{\mathcal{O}}(-A + \bar{H}\kappa/n_0R^2 - q^2\bar{H}\kappa/n_0) \\ -\bar{H}\kappa\Lambda(q^4 - q^2/R^2) & -Dq^2 \end{pmatrix} \begin{pmatrix} h \\ n \end{pmatrix}. \quad (6)$$

For the convex-anisotropic case the q^4 term in the lower left, and the q^2 term in the upper right vanish, while for concave-anisotropic case the terms proportional to $1/R^2$ in the lower left and upper right vanish.

Solving the coupled equations, we find the time dependence of the solution in the form: $e^{\omega(q)t}$, where $\omega(q) = \omega'(q) + i\omega''(q)$. The dispersion $\omega(q)$ can be solved analytically from Eq. 6, and is shown in Fig. 2 for the isotropic case, Fig. 3 for the convex-anisotropic case, and Fig. 4 for the concave-anisotropic case. We find that in a range of wavevectors, $q_{c,1} < q < q_{c,2}$, there is an instability $\omega'(q) > 0$, which is static laterally as $\omega''(q) = 0$ (Fig. 1 *d*). To better understand the behavior of the system, we plot $q_{c,1}$ and $q_{c,2}$ as functions of R (Fig. 2 *a*, Fig. 3 *a*, and Fig. 4 *a*) and A (Fig. 2 *b*, Fig. 3 *b*, and Fig. 4 *b*). The origin of the instability is clear: an aggregation of the CN causes the membrane to shrink toward the axis, therefore the local curvature becomes more positive and this draws more MP into the furrow, leading to an instability (Fig. 1 *d*). This is the mirror of the fingers-instability described in Gov and Gopinathan (10), and drives the aggregation of the CR, as we discuss below.

For a detailed description of the behavior shown in Figs. 2–4, see the Appendix. The values of the parameters used in these calculations are given in Table 1. The value of $\bar{H}$ corresponds to a spontaneous radius of the CN of 20 nm, which is reasonable for the curvature-sensing proteins that are currently known (16,34). The value of $An_0 \sim 10(\text{pN}/\mu\text{m}^2)$ (using the parameters of Table 1) should be smaller than the maximal force per unit area produced by a ring of close-packed myosin motors (each providing ~3 pN (35)). We can estimate this maximal force per unit area to be $P_{\max} \approx 10^4(\text{pN}/\mu\text{m}^2)$, so indeed our values are much lower than this

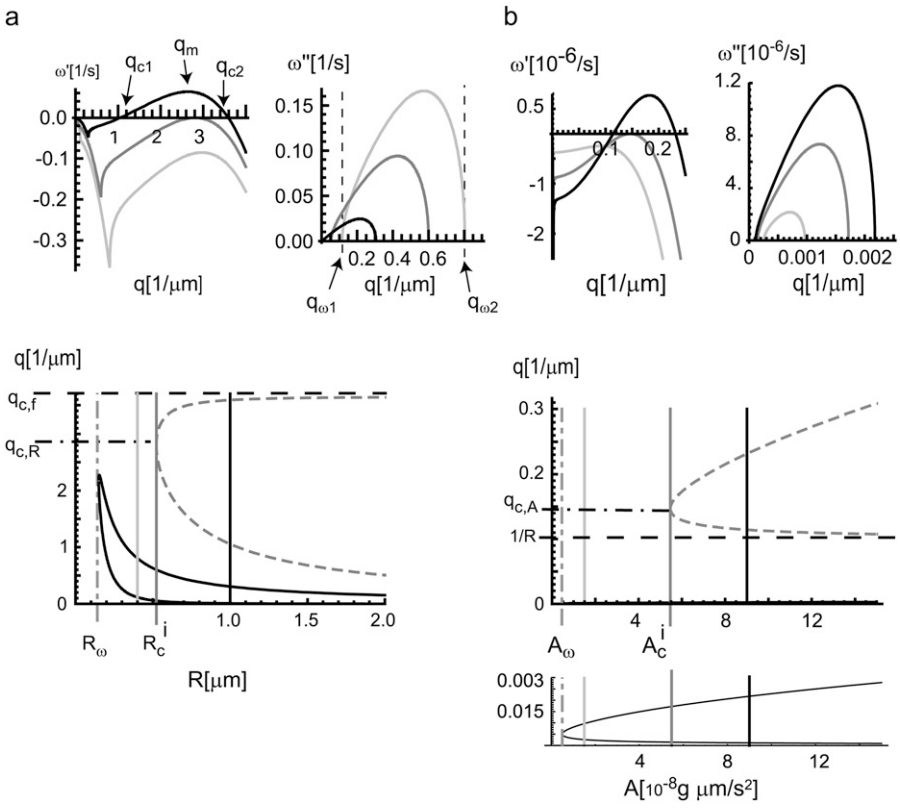

FIGURE 2 Solutions of the dispersion $\omega(q)$ from Eq. 6, for the isotropic case as a function of (*a*) R and (*b*) A. We plot both real and imaginary parts of $\omega(q)$. The shading of the lines in the top graphs corresponds to the values of R and A shown in the bottom graphs. The bottom graphs show the dependence of q_c (*dashed line*) and q_ω (*solid line*) on R and A. We denote the definitions of $q_{c,1}$, $q_{c,2}$, $q_{\omega,1}$, and $q_{\omega,2}$ in the top-left graphs. All graphs are at zero surface tension, and all the other parameters are given in Table 1. For the definitions of the critical values of A_ω and R_ω (*vertical dash-dot lines*), etc., see Concave Isotropic Case in the Appendix. The bottom-right panel shows the region of damped waves, which occur at much smaller values of q compared to the unstable regime (shown above).

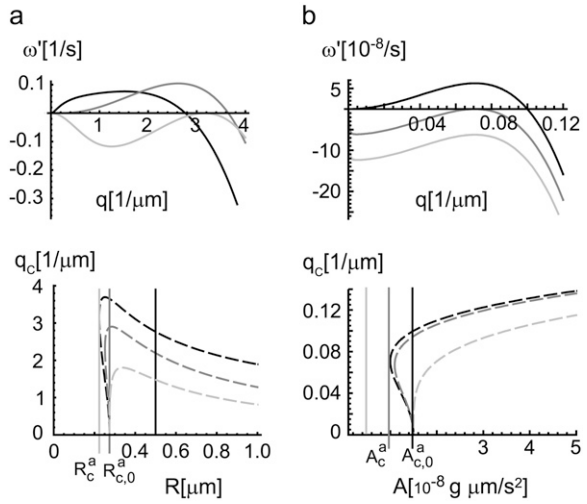

FIGURE 3 Solutions of the dispersion $\omega(q)$ from Eq. 6 for the convex-anisotropic case as a function of (*a*) R and (*b*) A. We plot the real part of $\omega(q)$ (the imaginary part is zero), at zero surface tension (corresponding to the *shaded line* in the *bottom graphs*). We follow the same shading scheme as in Fig. 2. (*Bottom panels*) The black dashed lines are for zero surface tension, while the shaded dashed lines are for different finite surface tensions of 5×10^{-5} gr/s^2 and 1.5×10^{-4}gr/s^2 $> \sigma_{c,1}$, respectively. For the definitions of the critical values A_c^a, etc., see Convex Anisotropic Case in the Appendix.

upper limit. For D we use a typical value of the diffusion coefficient inside the membrane (36), and $\Lambda = D/k_BT$ (31). Finally, the effective viscosity η takes into account the large friction in moving the membrane and the attached CN, while d is an estimate for the typical length-scale within the CN (25). Similarly, the value of the bending rigidity κ, which we chose to have a typical value appropriate for cellular membrane, can be very different from the value of the bare lipid membrane, due to the attached CN.

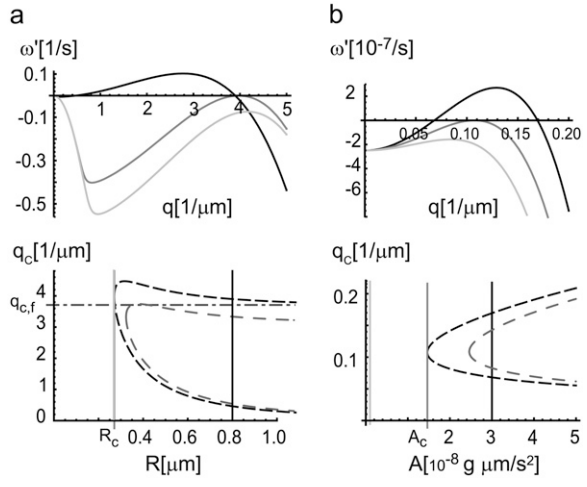

FIGURE 4 Solutions of the dispersion $\omega(q)$ from Eq. 6 for the concave-anisotropic case as a function of (*a*) R and (*b*) A. We plot the real part of $\omega(q)$ (the imaginary part is zero), at zero surface tension (corresponding to the *black dashed lines* in the *bottom graphs*). We follow the same shading scheme as in Fig. 2. The dashed shaded lines are for a finite surface tension 3×10^{-5}gr/s^2. For the definitions of the critical values A_c, etc., see Concave Anisotropic Case in the Appendix.

TABLE 1 List of the parameters used in the calculations

D [μm^2/s]	1	d [μm]	0.1
$\bar{H}$ [μM^{-1}]	50, −50	κ [k_BT]	2.5
η [G/μm s]	$100\eta_{water} = 10^{-4}$	A [gμm/s^2]	2×10^{-5}
Λ [S/g]	10^4	R [μm]	10
N_0 [1/μm^2]	10^3		

For $\bar{H}$, the first number corresponds to Figs. 2 and 4 and the second to Fig. 3. We chose A and n_0 so that the net contractile forces due to a cluster of size d^2 are of order: $An_0d^2 \sim 10^{-1}$ pN (77).

Note that the details of the proteins that are curvature-sensitive inside the contractile network (CN), are not fully characterized at present. Nevertheless, some curvature-sensing domains have been shown to have a spontaneous curvature of ~100–200 nm (34). We give these proteins as examples for possible curvature-sensing elements that may be part of the CN. The actual value of $\bar{H}$ may arise from the shape of a cluster of proteins (13), and not an individual protein, and therefore can be even larger. The CN will give rise to an instability as long as its spontaneous radius is smaller than that of the cell. Since cell radii are ~1–10 μm, this suggests that a spontaneous radius of ~0.1–0.5 μm is reasonable. In the above calculations, we used a typical value for the cell radius of $R \sim 10$ μm.

We wish to point out that disregarding the exact quantitative values of the parameters, our model provides a number of qualitative predictions: We show that the instability leading to the initiation of the CR does not occur when the radius is lower than a critical value, or the membrane tension is higher than a critical value (except for the convex anisotropic), or the contractile force is lower than a critical value (see Figs. 2–4, and the Appendix). This means that we expect these relations to hold, irrespective of the numerical values of the parameters. These general relationships are the main outcome of our model, as we describe below.

DISCUSSION OF THE MODEL RESULTS

We show above that, in an infinite cylinder, our model gives rise to unstable modes which provide a mechanism for the spontaneous aggregation of the CN into CRs. We now wish to describe how this instability can occur in a cell of finite length (Fig. 1 *d*). Let us emphasize that although we describe a process of spontaneous instability, the conditions that allow this instability to occur are highly regulated by the cell through control of all the model parameters: the contractile activity A, the length of free-membrane L, and the curvature sensitivity ($\bar{H}$). The last property is shown in Effler et al. (37).

Our model assumes that the components of the CN are localized in a band, usually along the cell equator, due to the action of various regulating agents, such as the microtubules

(MT) (38). These regulating agents determine the location and overall width of the band of CN (*light shaded stripe* in Fig. 5 *a*). Beyond this band, there are no CN elements on the membrane, due to various localization mechanisms. Inside this CN band, only the part which produces contractility and is free to deform, constitutes the free membrane of length L which we consider in our model (Fig. 5). Some parts of the CN band may be either inactive (i.e., not contractile), or prevented from deforming by physical constraints. Both effects can be related to the interaction of the CN with other cytoskeleton elements, such as the MT. This regulation is not fully understood at present and involves active transport of signaling and proteins along the MT (39), and the direct interaction of the MT with an acto-myosin cortical network (see further discussion in Cell Elongation and the Role of Microtubules).

Note that we do not deal here with the details of the aggregation of the CN band, but describe the conditions when this band (or part of it) becomes unstable and a CR is initiated. For example, the aggregation of the CN band does not seem to be dependent on the contractility (40), while the contractility A is essential for the initiation of the CR (instability), according to our model.

The constraints at the edges of the free membrane patch may be sharp or smooth, depending on the gradient of the regulating agents, such as the cortical MT. To simplify the solution we assumed here sharp boundary conditions at the edges of the free membrane patch, as this will not change the nature of our results. In the absence of the complex regulatory mechanisms, the whole cell surface which contains a cortical acto-myosin network can act as the free membrane. This occurs for example in unfertilized sea-urchin eggs, when the contractility is enhanced until a CR forms (41).

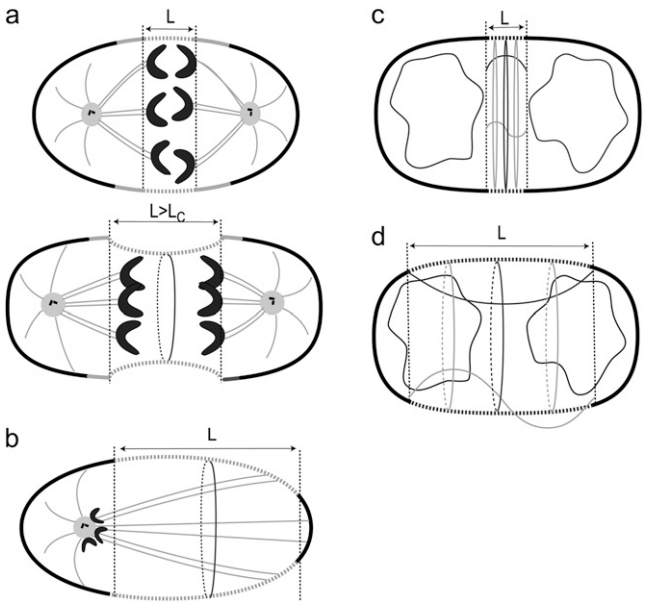

FIGURE 5 (*a* and *b*) Schematic picture of the location of the CN band (*light shaded stripe*), the definition of the free-membrane patch of length L (*dashed stripe*) and the formation of the CR when this patch becomes unstable. Note that L can be smaller than the width of the CN band. In panel *b*, we show the case of asymmetric division when one spindle pole is missing. In panel *c*, we show the cases where the CN band is highly concentrated between the nuclei due to cellular regulation (Type I). In panel *d*, we show the case when the CN is spread throughout the cell (Type II).

In a finite cylinder of length L the modes are limited to wavevectors with values $q_N = N\pi/L$, where N is an integer. Note that our calculation is for a purely cylindrical membrane, which is applicable for a short strip around an elongated cell's equator. When the cells are highly deformed and curved, this approximation of a cylindrical membrane may not be appropriate.

For a given value of contractile activity A and spontaneous curvature $\bar{H}$, as the cell becomes longer it moves along the trajectories shown in Fig. 6. We show two possible trajectories: a constant radius (*vertical arrow*) and a constant surface area, both for constant surface tension. (Note that in some cells there are measurements of increase in the membrane tension as the cell goes through mitosis (42).) We find that along these trajectories the cell reaches some critical length $L_c = \pi/q_{c,2}$ where the longest mode ($N = 1$) first becomes unstable (*bull's-eye* in Fig. 6).

Consider now a cell that has grown past its critical length L_c, so that the Nth mode becomes unstable (Fig. 6) at length NL_c. At long lengths, the constant surface-area trajectories shown in Fig. 6 take the cell back into the stable regime, when R becomes smaller than the critical radius (*vertical dashed line*). For the isotropic model, when $L \geq L_\omega = \pi/q_{\omega,2}$ (Fig. 6 *a*), damped oscillations appear (propagating waves). Note that in the isotropic and concave-anisotropic models (Fig. 6, *a* and *c*, respectively), each unstable mode N has a finite range of lengths in which it occurs, while for the convex-anisotropic model (Fig. 6 *b*), the modes remain unstable for all lengths above their critical length L_c.

Note that we can also consider the case of a cell with static geometry (fixed L and R) where the instability is triggered by a gradual increase in the activity of the CN, i.e., in A. This process is shown in Fig. 7, *a* and *b*, for the isotropic and convex-anisotropic cases, respectively. The critical value of A that triggers the instability can then be read off directly from these graphs.

The above linear analysis provides us with the mechanism for producing ring aggregation of CN along the cylindrical membrane, through the occurrence of unstable modes:

Type I. For the isotropic case, concave-anisotropic cases (Fig. 6, *a* and *c*) and for the convex-anisotropic case (when $\sigma < \sigma_{c,1}$) (Fig. 6 *b*), the instability occurs first for short lengths $L_c/R \sim 1$ (Fig. 5 *c*).

Type II. For the convex-anisotropic case when $\sigma > \sigma_{c,1}$ (*dashed lines* in Fig. 3) the instability occurs first for long lengths $L_c/R \gg 1$ (Fig. 5 *d*). Note that both these instabilities correspond to aggregates (rings) that are

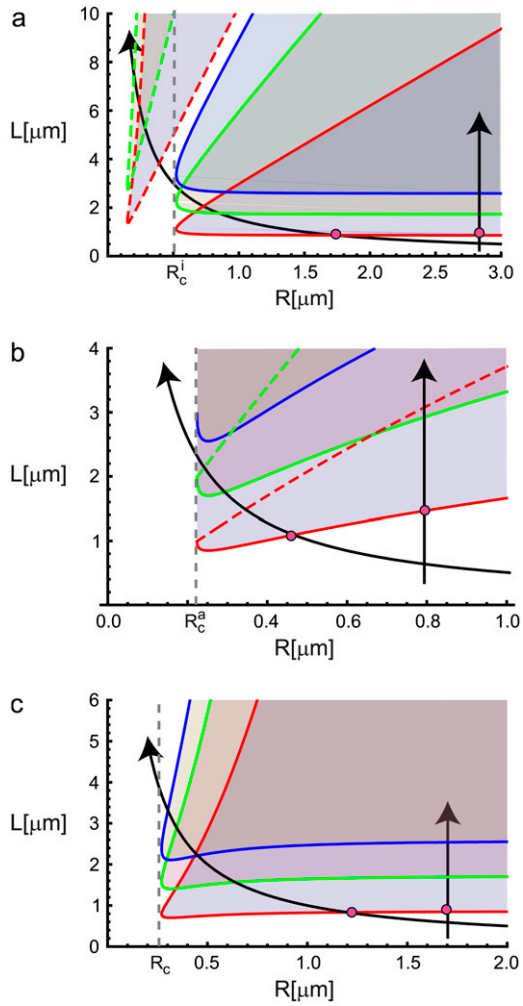

FIGURE 6 We plot the calculated critical cell lengths L_c as a function of the cell radius R, for the (*a*) isotropic, (*b*) convex-anisotropic, and (*c*) concave-anisotropic cases. In panels *a* and *c*, we also plot the upper critical length ($\pi/q_{c,1}$) so each mode is unstable inside these limits (*shaded regions*). In all the cases we show the trajectory of a cell that elongates while keeping a constant radius (*vertical arrow*), or with a constant surface area (*curved arrow*). The colors correspond to the different unstable modes: first mode, red; second mode, green; and third mode, blue. In panel *a*, we also plot the location of the transition to damped oscillatory solutions (L_ω), for the first two modes (*dashed lines*). In panel *b*, we plot in dashed lines the lengths $L_m = \pi/q_m$ where the first two modes are most unstable and $\omega'(q)$ is maximal (q_m gives the maximal value of the dispersion relation; see Fig. 3 *a*). The vertical dashed shaded lines give the critical radius for instability R_c^i, R_c^{a1}, and R_c^{a2}. The locations where the first mode becomes unstable are indicated by the bull's-eye on each trajectory.

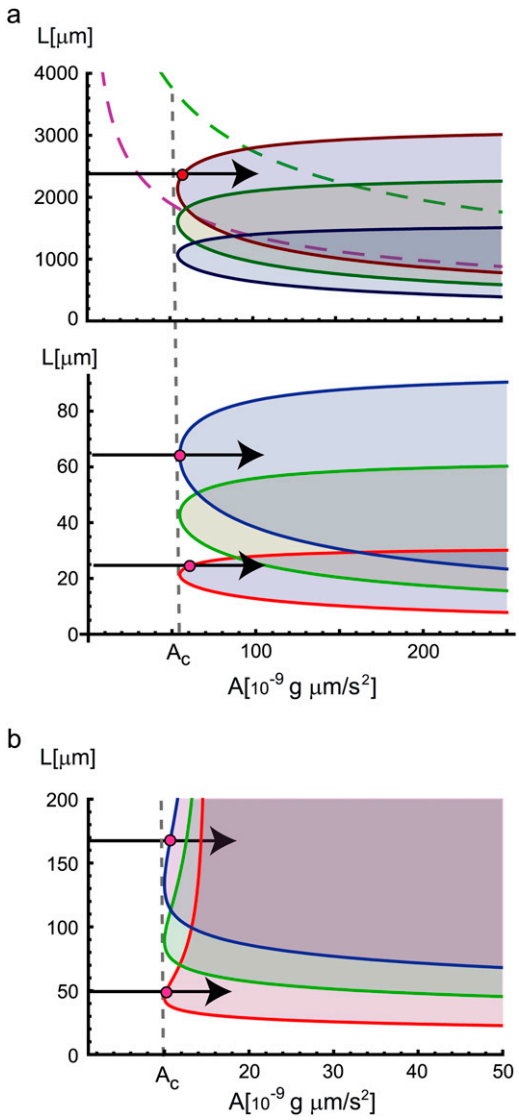

FIGURE 7 We plot the calculated critical cell lengths L_c as a function of the contractile activity A, for the (*a*) isotropic and (*b*) convex-anisotropic cases. We show the trajectory of a cell with fixed geometry and increasing contractility (*horizontal solid lines*). We follow the same color scheme as in Fig. 6. The vertical dashed shaded lines give the critical contractility for instability A_c^i and A_c^a. The locations where an instability or a propagating mode is initiated are indicated by the bull's-eye on each trajectory. Note that for the isotropic model (*a*) we give two figures to show the regime of instability of the first three modes (*bottom*) and the regime where the first two damped waves occur (*dashed lines* in the *upper figure*). The solid lines in the upper figure show the region of instability of the 25th mode (*dark blue*), 50th mode (*dark green*), and 100th mode (*purple*).

static laterally ($\omega''(q) = 0$, Figs. 2–4), as the CR are indeed observed to be in cells.

Type III. There is a third regime (Type III) in the isotropic case which exhibits damped oscillations (propagating waves), for lengths larger than L_ω (*dashed lines* in Fig. 6 *a*).

Below we compare the results of this analysis with the observed formation of CRs in different cells.

COMPARISON TO EXPERIMENTAL OBSERVATIONS

In this section, we compare the results of our model to the observed features of the CR in dividing eukaryotes. The nature of this comparison is mostly qualitative, since the quantitative values of key parameters that enter our model are unknown at present. Nevertheless, we wish to demonstrate

here the overall plausibility of our model and that it is in agreement with the observed qualitative characteristics of the CR initiation process.

We first wish to give some examples of specific types of proteins that may give the CN both its ability to produce contractility and its spontaneous curvature. In fission yeast, for example (25,29,30), the CN is composed of actin filaments that are linked by clusters containing myosin motors and a host of other proteins. One candidate, Formin-Cdc15 (16), is involved in both promoting the polymerization of actin filaments and provides anchorage to the membrane. This protein also contains the membrane-attachment domain F-BAR, which is known in other cases to produce spontaneous curvature (16). Another example is the combined effect of the Hob3p and Cdc42p clusters in yeast (43); the Hob3p provides anchorage to the membrane and may provide the spontaneous curvature (due to its BAR domain), while the Cdc42p promotes the polymerization of actin that connect the clusters to form the CN. The proteins of the CN are different in different cell types, and their exact role in ring formation is still being studied.

In the case of fission-yeast, the CN components are observed to aggregate not only at the furrow, where the ring eventually forms, but also at the hemispherical poles of the cell (8,44,45). This was most dramatically shown recently in Effler et al. (37), where the aggregation of myosin was triggered by aspiration into a micropipette, irrespective of the orientation of the chromosomes. This observation fits our convex-anisotropic model (Fig. 1, *a* and *c*), where the CNs aggregate at both the hemispherical caps and the middle furrow, once they are activated. Another observation links the ability of myosin-II to form long fibers, and their localization in both the furrow and the hemispherical caps (46). The specific proteins we list in the previous paragraph all have the BAR-domain, which has concave spontaneous curvature. Nevertheless, there was a recent discovery of a convex membranal protein that is involved in filopodia formation (34). These proteins contain a MIM-domain which has the convex shape, and proteins with this spontaneous curvature due to this domain may exist as components of the CN. It was further shown (37) that when the cell is not at the division stage of its lifecycle, these curvature-driven aggregations do not occur, presumably due to the inactivation of these protein clusters, which in our model corresponds to $A, \bar{H} \to 0$. These experiments show that our proposal that the membrane curvature serves as a cue for the aggregation of the CN, has experimental support. Note that the local surface tension may also play a role in the observed localization. (The exact manner in which the membrane curvature triggers the localization of myosin is not clear at the moment, and may involve a signaling that is triggered by the deformation. The simplest mathematical representation of such a system would be a quadratic Hamiltonian of the form of Eq. 1, even if now the parameters κ and $\bar{H}$ are effective representations of the underlying chemical reactions.)

Cell elongation and the role of microtubules

Once the cell is in the division stage, and the CN is activated (i.e., we have a finite A and $|\bar{H}|$), it still needs to reach the unstable region to trigger the initiation of the CR, according to our model. One possibility for this to occur is along the trajectories of Fig. 6, where there is an increase in the length of free membrane L, while the activity A is constant. In eukaryotes, there is a dramatic cell elongation before division, possibly due to the forces of the MTs that emanate from the two opposing spindles (47,48). The length L of free membrane where the aggregation of CN is allowed to occur and the membrane is free to deform, can be controlled by the internal structures of the cells, such as the MT asters, spindles, nuclei, and chromosomes (Fig. 5, *a*, *c*, and *d*), depending on the cell type. As these internal structures separate, the free membrane patch grows in length, until it reaches L_c, and the first mode becomes unstable (Fig. 6). This mode has maximal deformation and CN density at the midpoint between the two boundaries, and a ring forms at the center of the initial band (Fig. 5 *a*) (25,29). Therefore, within our model, the mechanism of the location of the ring is naturally solved (38).

In Fig. 3 of Hickson et al. (48), the timing of the appearance of the CR is delayed in cells that elongate more slowly, due to the suppression of a cytoskeleton element. The data seem to indicate that the appearance of the CR in both normal and modified cells occurs when they reach the same critical elongation. This observation is in agreement with our model of initiation of the CR when the CN becomes unstable beyond the critical length L_c (Fig. 6).

In our model, the formation of the CR is naturally synchronized to follow the separation of the internal cell structures that limit the length of the free membrane L, i.e., the MT-asters, nuclei, etc., depending on the cell type (38). Only when the length of free cell membrane between these separating structures is large enough does the membrane become unstable (Fig. 5 *a*). After the initiation of the CR, which our model describes, there is a condensation and coalescence into a tight ring (25,29). This is most likely driven by the contractile forces of myosin in the plane of the membrane (Fig. 1 *b*), and gives rise to nonlinear behavior (19–24), which is beyond our linear description.

The MT seem to play a key role in regulating the location, initial width, and activation of the CN on the cell membrane (49,50), in the region around the separating chromosomes or nuclei (Fig. 5 *a*). The exact mechanism of this regulation is not fully understood at present (51). It seems that in the cell there are two kinds of MTs that operate in parallel; some have the role of inhibiting the contractile activity of the cortical network (CN), while others are known to excite it. Together these MT serve to restrict the CN to a well-defined region of the membrane, which we call the free membrane. One possible mechanism for the MT to excite the CN may be by exerting a direct contractile force on the membrane where

they are attached to it. If the protein complex that attaches the MT ends to the membrane has also the spontaneous curvature that we assumed above, then its dynamics will exhibit the instability that we calculated.

In an experiment where both MT asters have been removed (52), the CR seems to appear at the geometrical midpoint of the cell, once the cell has elongated beyond some critical point. The cell elongation is driven by the growth of the remaining central MT. In other experiments one of the spindle was removed, and the remaining MT seem to elongate the deformed cell (53) until the CR appears, in this case shifted toward the spindle-free pole (Fig. 5 *b*). A similar observation was made in Bringmann and Hyman (54). Since the free membrane extends now from the remaining spindle to the opposing pole, we expect the first unstable mode to initiate a ring in this middle point (Fig. 5 *b*). In other cell types (more spread out) (55) this shift of the CR toward the free pole is less noticeable. The MT affect the cell asperity by elongation, increasing the ratio L/R, until instability occurs (Fig. 6, *a–c*). From these experiments, it seems that the CR can occur even in the absence of many components of the mitotic apparatus, but depends on the ability of MT to cause cell elongation. This is in accordance with our prediction that the CR initiation is influenced by the cell shape.

Note that in unfertilized sea-urchin egg cells (41), that have no MT spindles, a contractile ring forms at the cell center when the activity of myosin (and actin polymerization) is enhanced due to the introduction of Calyculin-A. Within our model this observation follows from the increase in A which decreases the critical length L_c, until the cell becomes unstable, even without the MT-induced elongation (Fig. 7, *a* and *b*).

Multiple and propagating rings

As shown in Figs. 6 and 7, a unique feature of our model is the prediction that higher order modes can also become unstable, which corresponds to the initiation of multiple rings (Fig. 5, *c* and *d*). Several examples that may fit this prediction are given below.

First, in abnormally long yeast cells, a wider band of CNs appear before cell division (56), and from these wider bands, multiple CRs appear. We expect that double rings will first appear when the length of CN (Fig. 5 *c*) is twice the critical length for the production of a single ring (Fig. 6, *a–c*). Indeed, the width of the CN band is found to be $\sim$2 larger in the mutant that has double rings, compared to the wild-type (Fig. 4, *A–C*, in (56)). In a mutant with a band that is only $\sim$1.5 larger than the wild-type, there is still only one CR forming, as our model predicts.

The second example comes from mutant yeast cells that have defective division-related proteins, and therefore grow to long lengths without division (8,57). In these cells, there is only an aggregation of CN components at the poles, representing a convex-anisotropic spontaneous curvature in our model. When these cells are induced to overexpress Myosin-I (8) or cdc15p (57), several bands of CR appear along the cell length. In our model we describe these cells as having initially very low (or zero) contractility A, and large length L. When they overexpress the CN components some contractility may be produced, and they follow the trajectories of Fig. 7, *a* and *b*. We therefore predict that these cells can give rise to bands with a high mode number ($N = 3$ seems to agree with the observed bands in the literature (8,57)). Since there are no separating nuclei in these cells, the entire length of the cell seems to be free for CN aggregation (Fig. 5 *d*).

In addition to multiple CR that are static laterally, our isotropic model gives rise to propagating (oscillating) damped modes (*upper trajectory* in Fig. 7 *a*). These modes may reflect the tendency to form propagating modes that, within the limitations of our cylindrical symmetry, correspond to the observed propagating spiral formations (8,40,48,57). Note that within our model we strictly calculate propagating rings, for wide (large L) and weakly contractile (small A) bands of CNs, in the isotropic concave case (Fig. 6 *a* and Fig. 7 *a*). (Another example of oscillatory behavior of the cortical acto-myosin network is given in (58). These systems are different from dividing cells, as they do not exhibit a localization of the acto-myosin in the ringlike constriction, but rather form a continuous hemispherical cap on one side of the furrow.)

Two experimental observations of such wavelike contractions and multiple rings are the following:

1. In disrupted *C. elegans* embryos that have small MT asters (59), there is no confinement of the CN, and as a result, its components are smeared over the entire cell membrane. We are therefore in the conditions of large L and small A, which can give rise, according to our model (Fig. 7, *a* and *b*), to the observed multiple contraction furrows (59).
2. In dividing sea-urchin cells (60), it is observed that when the CN band is artificially widened (by disrupting the MT, or by physically moving the MT asters), or disrupted (by actin depolymerization), the CR initiation is modified and propagating ruffles appear instead. These manipulations of the cell again correspond to an increase in L and a decrease in A.

Cell geometry

Our model predicts that the critical width L_c of the CN will depend on the radius of the cell, as shown in Fig. 6; the dependence is very weak for the isotropic and concave-anisotropic models (Fig. 6, *a* and *c*), while it is significant for the convex-anisotropic model (Fig. 6 *b*). We wish to compare our calculation convex-anisotropic model with the observed behavior, which comes from two different independent experiments, and is shown in Fig. 8.

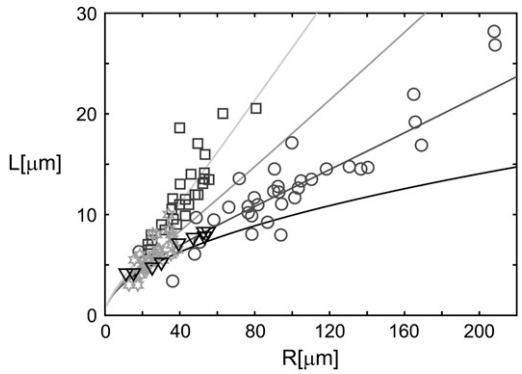

FIGURE 8 Calculation of the furrow initiation time using our convex-anisotropic model, as a function of the cell radius, compared to observations. Solid triangles (49), green (*shaded stars*) and purple (*shaded squares*) sea urchin, and in *X. laevis embryo* (*shaded circles*) (60). In ascending shading: $\sigma = 0$ (*solid line*), $\sigma = 10^{-6}$g/s^2, $\sigma = 3 \times 10^{-6}$g/s^2, and $\sigma = 7 \times 10^{-6}$g/s^2. The parameters used in this fit are $A = 2 \times 10^{-4}$ [gμm/s^2], and the rest are given in Table 1.

In the first experiment (49), sea-urchin egg cells were manipulated in a capillary pipette of varying radius. The cells are therefore constrained to have the radius of the pipette, and the onset time of furrowing was observed to decrease with decreasing radius. This onset time was measured from the instant of chromosome separation, which move apart at a velocity of $\sim$1.2 μm/min (49). Using this velocity we can therefore determine from the onset time the physical separation of the chromosomes, which we take to be close to the width of the free-membrane patch L (see discussion in previous section, and Fig. 5 *a*). According to our model, at the onset of furrowing this width is equal to the critical length L_c. The trajectory for a cell in such a geometry is that of fixed radius and increasing L (*vertical arrow* in Fig. 6 *b*).

The second experiment (60) gives the observed width of the cortical band of active RhoA (60), which is an indication for the width of the CN. The width of the free membrane L is bounded by this length, and it is therefore reasonable to use this value as an estimate for the critical length for furrowing, i.e., L_c. In these experiments, we estimate the cell radius as given by half the measured pole-to-pole distance (60).

In Fig. 8, we compare the experimental data of both experiments to our calculated critical length. Note that there is good agreement between the data of both experiments, which indicates that the separation of the chromosomes correlated very well with the width of the active RhoA cortical band. There is also good agreement between the data from the two different species. Our model predicts (Eq. 7) a transition from a $\sqrt{R}$ to a linear dependence as the surface tension increases, and this may be indicated by the data. Overall, our convex-anisotropic model gives a very good description of the data from both experiments.

The surface tension which we use to fit the observations in Fig. 8 is a low value which is consistent with simple finite membrane area consideration, i.e., $\sigma \sim \kappa/R^2$. Furthermore, cells seem to use an exocytosis process during cytokinesis (61) to maintain a low value of surface tension. If the surface tension is not maintained at a low value but increases, this can lead to a suppression of the CR initiation; for the convex-anisotropic model, the critical length $L_c/R \propto \sqrt{\sigma}$ increases with σ, until it can be longer than the cell length. These predictions remain to be tested. In Effler et al. (37), it is observed that cells in very narrow pipettes, radius of 2–3 μm, sometimes fail to divide. This may indicate that above a critical surface tension there is no instability, as our model predicts. Note that the minimal critical radius below which there is no cleavage at all, is very small using these parameters (Fig. 6 *b*). If the contractility A is lowered using certain toxins, the value of the critical radius increases (see Appendix, Convex Anisotropic Case) and may be observed in micropipette experiments (37,49).

CONCLUSION

Our proposed model shows that there can be a general mechanism that gives rise to aggregation of ringlike membrane proteins, which may correspond to the formation of the CR. In our model, the main cue that correlates the membrane shape with the recruitment of contractile-ring elements, is the local curvature. Our model therefore gives a crucial role to the structural features of the membranal complexes that form the CR, as is indicated in recent molecular studies (62). We propose that one of the important structural features of these proteins is their spontaneous curvature. It remains to be tested if indeed there are curvature-sensitive components in the CR, as our model proposes, and a detailed characterization of them.

Our model should be applicable to a wide range of biological systems, due to its general features. This model predicts that dynamic instability can occur whenever there is a coupling between the membrane curvature and contractile forces, and should therefore be applicable to many biological circumstances. For example, in prokaryotes the CR is composed of bundles of FtsZ filaments and host proteins. Assuming that these bundles have a spontaneous curvature and produce a contractile force, then the initiation of the CR in these cells may follow our proposed mechanism as well. The origin of such contractile forces may be the process of GTP hydrolysis that causes the FtsZ filaments to curve inwards and therefore apply a contractile force to the membrane (63–66). Similarly, in subcellular organelles inside eukaryotes, the prokaryotic proteins that form the CR in bacteria perform similar functions, leading to fission phenomena (63,67). Certain mutant bacteria do not form functional CR but exhibit propagating, short-lived structures (rings and spirals) (68,69), which may correspond to the damped propagating solutions that we found above (Fig. 2).

Another example of cell division comes from budding-yeast (70). Here a ring forms at an early stage around the neck of a membrane bud, even before DNA replication. We

propose that it is the local curvature at the neck of the bud that attracts the relevant membrane proteins there. In certain multinucleated organisms (*A. nidulans*) there are compartments called septa, which are observed to form at a uniform separation along long cellular protrusions (71). This uniformity, and the observed role of cell length in the initiation of the division process, may indicate that a similar process to the one described by our model takes place.

In fission yeast, the nucleus divides before the overall division of the cell (72). The elongation of the nucleus after DNA replication is driven by the growth of internal MT (73). The final division of the elongated nucleus is not understood at present, and may be driven by a contractile instability of the type that we propose in this article.

The idea that mechanical instability is the driving mechanism for the initiation of the CR in dividing cells is not new, and has been proposed in other models (19–24). Our model is the first to couple the membrane shape with the contractile forces of the cytoskeleton to produce an instability at the cell membrane. Furthermore, the proposed model provides a general mechanism of which cells may take advantage when initiating the CR, although the specific proteins used in each cell type can be very different. What we propose is that despite the differences these membrane proteins may all share similar characteristics, namely a specific spontaneous curvature and contractile activity. In addition, there are certainly other possibilities for producing cell division which may be unrelated to our proposed instability mechanism, and that cells use under different conditions, such as in drug-treated or adherent cells (74,75).

In this article, we restrict the treatment of our model to the linear regime, so that analytic results and deeper understanding of the behavior is extracted. (Note that, for future work, the nonlinear terms may be calculated to make the comparisons with experiments more realistic.)

The initiation of the CR may indeed result from a nonlinear mechanism, but our model shows that it may also be the result of a linear instability phenomena. Note that the instability we describe in this article can also drive the phase separation of membrane components in the furrow of dividing cells (9), similar to the mechanism described in Veksler and Gov (76).

To test the validity of our proposed mechanism, we list the following predictions:

1. Increasing the surface tension σ in the cell membrane (for example, by increasing the osmotic pressure in the cell) should restrict the appearance of the contractile ring to larger free membrane lengths $L_c \propto \sqrt{\sigma}$ (in the convex-anisotropic case, Fig. 8, *a* and *b*), or even suppress it completely above some critical tension (for the isotropic and concave-anisotropic cases).
2. Cylindrical cells of different radii should exhibit division at different critical lengths, with L_c monotonously increasing with R (Fig. 6).
3. We predict that decreasing the contractile forces will lead to an increase in the critical length before division, and below some critical value will prevent the formation of the CR (Fig. 7). This may be achieved in eukaryotes by partially blocking the activity of myosin (77).
4. Constraining the cell to a small radius below some critical value (Fig. 6), or increasing its surface tension, will inhibit ring formation, as can be tested experimentally (37,49).
5. Concerning the appearance of propagating modes (spirals), we predict from our isotropic model (Fig. 2) that these will appear only in some range of weak contraction ($A_\omega < A < A_c^i$) or small radii ($R_\omega < R < R_c^i$). The critical contraction A_c^i is inversely dependent on the radius squared, which may be tested experimentally.
6. Placing unfertilized sea-urchin egg (41) in a pipette of varying radius, and with different concentrations of Calyculin-A, may allow us to scan the critical conditions for CR initiation in the $R - A$ plane.

APPENDIX

In this Appendix, we give a detailed description of the behavior of the critical wavevectors shown in Figs. 2 and 3.

Concave isotropic case

As $R \rightarrow \infty$, the system becomes flat (10): $q_{c,1} \rightarrow 0$ and $q_{c,2} \rightarrow q_{c,f} \equiv \sqrt{(A\bar{H}\kappa\Lambda - \sigma D)/\kappa\alpha}$ (shown as the *horizontal dashed line* in Fig. 2 *a*), where $\alpha \equiv D - \bar{H}^2\kappa\Lambda/n_0$. (Note that, throughout this article, we assume that α, which is the difference between the diffusion and the passive aggregation due to the spontaneous curvature, is always positive. Otherwise, the system becomes unstable even without the active forces, for all wavevectors.) Below a critical radius R_c^i, there is no longer instability, since the large negative curvature of the thin cylinder dominates and there is no advantage for the CN to come closer to the axis. For the case of $\sigma = 0$, we get a simple solution for the critical radius which shows instability, $R_{c,0}^i = \sqrt{(2\sqrt{D\alpha}+D)/A\bar{H}\Lambda}$, with wavevector $q_{c,R} = \sqrt{(1+D(2\alpha+\sqrt{\alpha D})/\alpha(D+2\sqrt{\alpha D})}/R_{c,0}^i$. At the critical radius R_c^i, the forces leading to instability (spontaneous curvature and contraction) balance the forces leading to stability (diffusion and membrane elasticity). As the surface tension increases, the critical radius increases $R_c^i \propto (\sigma - \sigma_{c,i})^{-1}$ and $q_{c,f}$ decreases, until a critical surface tension, $\sigma_{c,i} = A\bar{H}\kappa\Lambda/D$, above which there is no instability ($q_{c,2} = 0$ at all radii).

In Fig. 2 *b*, we plot the solution as a function of A. We find that as A becomes smaller the unstable region shrinks until it disappears below a critical value, $A_{c,0}^i = -(D - 2\sqrt{D\alpha})/\bar{H}\Lambda R^2$ (for $\sigma = 0$), with wavevector $q_{c,A} = \sqrt{(1+\sqrt{D/\alpha})}/R$. Both R_c^i and A_c^i occur when the timescale for CN diffusion $\sim R^2/D$ equals the active aggregation time $\sim 1/A\bar{H}\Lambda$. When either R or A decreases below the critical values, the diffusion is faster than the active aggregation and no instability occurs. In the limit of $A \rightarrow -\infty$, the unstable region expands as $q_{c,1} \rightarrow 1/R$ and $q_{c,2} \rightarrow \sqrt{A\bar{H}\Lambda/\alpha}$.

At wavevectors $q_{\omega,1} < q < q_{\omega,2}$ we find a stable region with damped oscillations ($\omega'(q) < 0$ and $\omega''(q) \neq 0$) (Fig. 2). For these long wavelengths, it is energetically unfavorable for the CN to come close to the cylindrical axis where the curvature is negative for a straight cylinder. We therefore have a situation which is similar to the damped waves in the flat case with protrusive forces (10). The range of wavevectors that exhibit damped

oscillations grow when R decreases (Fig. 2 *a*). Eventually, below R_ω the spontaneous curvature of the membrane dominates, given by κ/R^4 in the top left term of Eq. 6, and the oscillations disappear. A similar behavior is found as a function of A (Fig. 2 *b*), where the oscillatory region vanishes below a critical value of A_ω. In the limit of small q, $\sigma = 0$ and $D \ll \kappa\hat{\mathcal{O}}$, we get $R_\omega \simeq (\kappa\hat{\mathcal{O}}/A\bar{H}\Lambda)^{1/4}$ and $A_\omega \simeq -\kappa\hat{\mathcal{O}}/R^4\bar{H}\Lambda$. From these expressions, we find that the disappearance of the oscillations occurs when the membrane response time $\sim R^4/\kappa\hat{\mathcal{O}}$ is faster than the active aggregation time. In the limit $A \to \infty$, the oscillatory region approaches a finite strip where $q_{\omega,1} \propto 1/\sqrt{A}$ and the upper limit approaches the lower limit of the unstable region $q_{\omega,2} \to q_{c,1} \to 1/R$ (shown as the *horizontal dashed line* in Fig. 2 *b*). In the flat limit $R \to \infty$, the oscillatory region vanishes as $q_{\omega,2} \to \sqrt{4A\bar{H}\kappa\Lambda\hat{\mathcal{O}}/(D-\sigma\hat{\mathcal{O}})^2}/R$ and $q_{\omega,1} \propto 1/R^3$. Note that at $q = 1/R$ we find that ω' is independent on A.

Convex anisotropic case

We now describe the convex-anisotropic case (Fig. 3). There is a range of wavevectors $q_{c,1} < q < q_{c,2}$ with unstable modes, which are static laterally. In the limit of large R, we find $q_{c,1} = 0$ and $q_{c,2}$ vanishes as (in the limit $R \to \infty$)

$$q_{c,2} \to \sqrt{A|\bar{H}|\kappa\Lambda/\sigma D}/R,\ \sigma \neq 0,$$

$$q_{c,2} \to (A|\bar{H}|\Lambda/D)^{1/4}/\sqrt{R},\ \sigma = 0. \quad (7)$$

As R becomes smaller the unstable region widens, but eventually the spontaneous curvature of the cylindrical membrane dominates and the unstable region disappears.

For surface tension smaller than a critical value, $\sigma^{R}_{c,1} = A\bar{H}\kappa\Lambda/\alpha$, the unstable region persists down to a critical radius R^{a1}_c, which is always smaller than the radius $R^{a}_{c,0} = \sqrt{\alpha/A\bar{H}\Lambda}$, which is where $q_{c,1}$ vanishes (Fig. 3 *a*).

As a function of A, we find a similar behavior; for large A we have $q_{c,1} = 0$ and $q_{c,2} \to \sqrt{A\bar{H}\Lambda/DR^2 4}$ in the limit $A \to \infty$ (Fig. 3 *b*). When A decreases, the unstable region shrinks and eventually disappears.

For surface tension smaller than $\sigma^{A}_{c,1} = \kappa/R^2$ the instability vanishes below $A^{a}_c = (4\kappa^2\alpha - D(\kappa - R^2\sigma)^2)/4\bar{H}R^2\kappa^2\Lambda$, which is smaller than $A^{a}_{c,0} = \alpha/\bar{H}\Lambda R^2$, where $q_{c,1}$ vanishes. Note that as the surface tension increases above $\sigma_{c,1}$ the unstable region occurs only for $R > R^{a}_{c,0}$ and $A > A^{a}_{c,0}$ but persists for all values of the surface tension (unlike the isotropic case). For the convex-anisotropic case, there is no driving force for oscillatory solutions, since the CN always aggregate where the local radius of the membrane is smallest.

Concave anisotropic case

We now describe the concave-anisotropic case (Fig. 4). As for the previous case, we find unstable modes at $q_{c,1} < q < q_{c,2}$, which are static laterally. In the limit of large R (Fig. 4 *a*) we find $q_{c,1} \to 1/R$, and $q_{c,2}$ approaches the constant value for flat membranes (10): $q_{c,2} \to \sqrt{(A\bar{H}\kappa\Lambda - \sigma D)/\kappa\alpha}$. As R becomes smaller, the unstable region shrinks, and eventually the spontaneous curvature of the cylindrical membrane dominates and the unstable region disappears. For surface tension larger than a critical value, $\sigma_{c,2} = A\bar{H}\kappa\Lambda/D$, the unstable region vanishes. The critical radius below which the system is stable is given by (for zero surface tension): $R^{a2}_c = \sqrt{(-D + 2\sqrt{D\alpha})/A\bar{H}\Lambda}$.

As a function of A we have $q_{c,1} \to 0$ and $q_{c,2} \propto \sqrt{A\bar{H}\Lambda/\alpha}$ in the limit of large A (Fig. 4 *b*). When A decreases, the unstable region shrinks and eventually disappears, at A_c. For the concave-anisotropic case, there is no driving force for oscillatory solutions.

We thank Fred Chang for useful discussions and many helpful comments. We thank Mario Feingold for useful discussions and Tsvi Tlusty for comments.

We thank the European Union SoftComp NoE grant, the Robert Rees Fund for Applied Research, and the Alvin and Gertrude Levine Career Development Chair, for their support. This research was supported by the Israel Science Foundation (grant No. 337/05).

REFERENCES

1. Scholey, J. M., I. Brust-Mascher, and A. Mogilner. 2003. Cell division: cytoskeleton. *Nature*. 422:746–752.
2. Robinson, D. N., and J. A. Spudich. 2000. Towards a molecular understanding of cytokinesis. *Trends Cell Biol*. 10:228–237.
3. Dean, S. O., S. L. Rogers, N. Stuurman, R. D. Vale, and J. A. Spudich. 2005. Distinct pathways control recruitment and maintenance of myosin II at the cleavage furrow during cytokinesis. *Proc. Natl. Acad. Sci. USA*. 102:13473–13478.
4. Nanninga, N. 2001. Cytokinesis in prokaryotes and eukaryotes: common principles and different solutions. *Microbiol. Mol. Biol. Rev*. 65: 319–333.
5. Emoto, K., T. Kobayashi, A. Yamaji, H. Aizawa, I. Yahara, K. Inoue, and M. Umeda. 1996. Redistribution of phosphatidylethanolamine at the cleavage furrow of dividing cells during cytokinesis. *Proc. Natl. Acad. Sci. USA*. 93:12867–12872.
6. Umeda, M., and K. Emoto. 1999. Membrane phospholipid dynamics during cytokinesis: regulation of actin filament assembly by redistribution of membrane surface phospholipids. *Chem. Phys. Lipids*. 101: 81–91.
7. An, M. W., W. Z. Wu, and W. Y. Chen. 2005. Membrane phospholipid redistribution in cytokinesis: a theoretical model. *Acta Biochim. Biophys. Sin. (Shanghai)*. 37:643–648.
8. Takeda, T., and F. Chang. 2005. Role of fission yeast Myosin I in organization of sterol-rich membrane domains. *Curr. Biol*. 15:1331–1336.
9. Ng, M. M., F. Chang, and D. R. Burgess. 2005. Movement of membrane domains and requirement of membrane signaling molecules for cytokinesis. *Dev. Cell*. 9:781–790.
10. Gov, N., and A. Gopinathan. 2006. Dynamics of membranes driven by actin polymerization. *Biophys. J*. 90:454–469.
11. Roux, A., D. Cuvelier, P. Nassoy, J. Prost, P. Bassereau, and B. Goud. 2005. Role of curvature and phase transition in lipid sorting and fission of membrane tubules. *EMBO J*. 24:1537–1545.
12. Parthasarathy, R., C. H. Yu, and J. T. Groves. 2006. Curvature-modulated phase separation in lipid bilayer membranes. *Langmuir*. 22: 5095–5099.
13. Zimmerberg, J., and M. M. Kozlov. 2006. How proteins produce cellular membrane curvature. *Nat. Rev. Mol. Cell Biol*. 7:9–19.
14. Iglič, A., T. Slivnika, and V. Kralj-Iglič. 2007. Elastic properties of biological membranes influenced by attached proteins. *J. Biomech*. 40: 2492–2500.
15. Iglič, A., B. Babnika, K. Bohinca, M. Fošnarič, H. Hägerstrand, and V. Kralj-Iglič. 2007. On the role of anisotropy of membrane constituents in formation of a membrane neck during budding of a multicomponent membrane. *J. Biomech*. 40:579–585.
16. Itoh, T., and P. D. Camilli. 2006. BAR, F-BAR (EFC) and ENTH/ANTH domains in the regulation of membrane-cytosol interfaces and membrane curvature. *Biochim. Biophys. Acta*. 1761:897–912.
17. Huang, K. C., R. Mukhopadhyay, and N. S. Wingreen. 2006. A curvature-mediated mechanism for localization of lipids to bacterial poles. *PLoS Comput. Biol*. 2:1357–1364.
18. Tsafrir, I., D. Sagi, T. Arzi, M. A. Guedeau-Boudeville, V. Frette, D. Kandel, and J. Stavans. 2001. Pearling instabilities of membrane tubes with anchored polymers. *Phys. Rev. Lett*. 86:1138–1141.
19. Wang, Y. L. 2001. The mechanism of cytokinesis: reconsideration and reconciliation. *Cell Struct. Funct*. 6:633–668.
20. Wang, Y. L. 2005. The mechanism of cortical ingression during early cytokinesis: thinking beyond the contractile ring hypothesis. *Trends Cell Biol*. 15:581–588.

21. Greenspan, H. P. 1977. On the dynamics of cell cleavage. *J. Theor. Biol.* 65:79–99.
22. Zinemanas, D., and A. Nir. 1988. On the viscous deformation of biological cells under anisotropic surface tension. *J. Fluid Mech.* 193: 217–241.
23. An, M., W. Wu, and W. C. WY, 2005. Membrane phospholipid redistribution in cytokinesis: a theoretical model. *Acta Biochim. Biophys. Sinica.* 37:643–648.
24. White, J. G., and G. G. Borisy. 1983. On the mechanisms of cytokinesis in animal cells. *J. Theor. Biol.* 101:289–316.
25. J.-Q. Wu, V. Sirotkin, D. R. Kovar, M. Lord, C. C. Beltzner, J. R. Kuhn, and T. D. Pollard. 2006. Assembly of the cytokinetic contractile ring from a broad band of nodes in fission yeast. *J. Cell Biol.* 174: 391–402.
26. Zumdieck, A., M. C. Lagomarsino, C. Tanase, K. Kruse, B. Mulder, M. Dogterom, and F. Jülicher. 2005. Continuum description of the cytoskeleton: ring formation in the cell cortex. *Phys. Rev. Lett.* 95: 258103.
27. Biron, D., E. Alvarez-Lacalle, T. Tlusty, and E. Moses. 2005. Molecular model of the contractile ring. *Phys. Rev. Lett.* 95:098102.
28. Zhang, W., and D. N. Robinson. 2005. Balance of actively generated contractile and resistive forces controls cytokinesis dynamics. *Proc. Natl. Acad. Sci. USA.* 102:7186–7191.
29. Wu, J. Q., J. R. Kuhn, D. R. Kovar, and T. D. Pollard. 2003. Spatial and temporal pathway for assembly and constriction of the contractile ring in fission yeast cytokinesis. *Dev. Cell.* 5:723–734.
30. Eggert, S. U., T. J. Mitchison, and C. M. Field. 2006. Animal cytokinesis: from parts list to mechanisms. *Annu. Rev. Biochem.* 75: 543–566.
31. Manneville, J. B., P. Bassereau, S. Ramaswamy, and J. Prost. 2001. Active membrane fluctuations studied by micropipette aspiration. *Phys. Rev. E.* 64:021908.
32. Ramaswamy, S., J. Toner, and J. Prost. 2000. Nonequilibrium fluctuations, traveling waves, and instabilities in active membranes. *Phys. Rev. Lett.* 84:3494–3497.
33. Safran, S. A. 2003. Statistical Thermodynamics of Surfaces, Interfaces, and Membranes, 1st Ed. Westview Press, Boulder, CO.
34. Mattila, P. K., A. Pykalainen, J. Saarikangas, V. O. Paavilainen, H. Vihinen, E. Jokitalo, and P. Lappalainen. 2007. Missing-in-metastasis and IRSp53 deform PI(4,5)P2-rich membranes by an inverse BAR domain-like mechanism. *J. Cell Biol.* 176:953–964.
35. Finer, J. T., R. M. Simmons, and J. A. Spudich. 1994. Single myosin molecule mechanics: picoNewton forces and nanometer steps. *Nature.* 368:113–119.
36. Almeida, P. F. F., and W. L. C. Vaz. 1995. Handbook of Biological Physics, Vol. 1. Elsevier Science, Amsterdam, The Netherlands.
37. Effler, J. C., Y. S. Kee, J. M. Berk, M. N. Tran, P. A. Iglesias, and D. N. Robinson. 2006. Mitosis-specific mechanosensing and contractile-protein redistribution control cell shape. *Curr. Biol.* 16:1962–1967.
38. Margolin, W., and R. Bernander. 2004. How do prokaryotic cells cycle? *Curr. Biol.* 14:R768–R770.
39. Straight, A. F., and C. M. Field. 2000. Microtubules, membranes and cytokinesis. *Curr. Biol.* 10:R760–R770.
40. Straight, A. F., A. Cheung, J. Limouze, I. Chen, N. J. Westwood, J. R. Sellers, and T. J. Mitchison. 2003. Dissecting temporal and spatial control of cytokinesis with a Myosin II inhibitor. *Science.* 299:1743–1747.
41. Tosuji, H., K. Miyaji, N. Fusetani, and T. Nakazawa. 2000. Effect of calyculin A on the surface structure of unfertilized sea urchin eggs. *Cell Motil. Cytoskeleton.* 46:129–136.
42. Raucher, D., and M. Sheetz. 1999. Membrane expansion increases endocytosis rate during mitosis. *J. Cell Biol.* 144:497–506.
43. Coll, P. M., S. A. Rincon, R. A. Izquierdo, and P. Perez. 2007. Hob3p, the fission yeast ortholog of human BIN3, localizes Cdc42p to the division site and regulates cytokinesis. *EMBO J.* 26:1865–1877.
44. Pelham, R. J., and F. Chang. 2002. Actin dynamics in the contractile ring during cytokinesis in fission yeast. *Nature.* 419:82–86.
45. Tasto, J. J., J. L. Morrell, and K. L. Gould. 2003. An anillin homologue, Mid2p, acts during fission yeast cytokinesis to organize the septin ring and promote cell separation. *J. Cell Biol.* 160:1093–1103.
46. Shu, S., X. Liu, and E. D. Korn. 2003. *Dictyostelium* and *Acanthamoeba* myosin II assembly domains go to the cleavage furrow of *Dictyostelium* myosin II-null cells. *Proc. Natl. Acad. Sci. USA.* 100:6499–6504.
47. Robinson, D. N., and J. A. Spudich. 2004. Mechanics and regulation of cytokinesis. *Curr. Opin. Cell Biol.* 16:182–188.
48. Hickson, G. R. X., A. Echard, and P. H. O'Farrell. 2006. Rho-kinase controls cell shape changes during cytokinesis. *Curr. Biol.* 16:359–370.
49. Shuster, C. B., and D. R. Burgess. 2002. Transitions regulating the timing of cytokinesis in embryonic cells. *Curr. Biol.* 12:854–858.
50. Strickland, L. I., E. J. Donnelly, and D. R. Burgess. 2005. Induction of cytokinesis is independent of precisely regulated microtubule dynamics. *Mol. Biol. Cell.* 16:4485–4494.
51. Rodriguez, O. C., A. W. Schaefer, C. A. Mandato, P. Forscher, W. M. Bement, and C. M. Waterman-Storer. 2003. Conserved microtubule-actin interactions in cell movement and morphogenesis. *Nat. Cell Biol.* 5:599–609.
52. Alsop, G. B., and D. Zhang. 2003. Microtubules are the only structural constituent of the spindle apparatus required for induction of cell cleavage. *J. Cell Biol.* 162:383–390.
53. Alsop, G. B., and D. Zhang. 2004. Microtubules continuously dictate distribution of actin filaments and positioning of cell cleavage in grasshopper spermatocytes. *J. Cell Sci.* 117:1591–1602.
54. Bringmann, H., and A. A. Hyman. 2005. A cytokinesis furrow is positioned by two consecutive signals. *Nature.* 436:731–734.
55. Canman, J. C., L. A. Cameron, P. S. Maddox, A. Straight, J. S. Tirnauer, T. J. Mitchison, G. Fang, T. M. Kapoor, and E. D. Salmon. 2003. Determining the position of the cell division plane. *Nature.* 424: 1074–1078.
56. Padte, N. N., S. G. Martin, M. Howard, and F. Chang. 2006. The cell-end factor Pom1p inhibits Mid1p in specification of the cell division plane in fission yeast. *Curr. Biol.* 16:2480–2487.
57. Takeda, T., T. Kawate, and F. Chang. 2004. Organization of a sterol-rich membrane domain by cdc15p during cytokinesis in fission yeast. *Nat. Cell Biol.* 6:1142–1144.
58. Paluch, E., J. van-der Gucht, J. F. Joanny, and C. Sykes. 2006. Deformations in actin comets from rocketing beads. *Biophys. J.* 91: 3113–3122.
59. Motegi, F., N. V. Velarde, F. Piano, and A. Sugimoto. 2006. Two phases of astral microtubule activity during cytokinesis in *C. elegans* embryos. *Dev. Cell.* 10:509–520.
60. Bement, W. M., H. A. Benink, and G. von Dassow. 2005. A microtubule-dependent zone of active RhoA during cleavage plane specification. *J. Cell Biol.* 170:91–101.
61. Shuster, C. B., and D. R. Burgess. 2002. Targeted new membrane addition in the cleavage furrow is a late, separate event in cytokinesis. *Proc. Natl. Acad. Sci. USA.* 99:3633–3638.
62. Lister, I. M., N. J. Tolliday, and R. Li. 2006. Characterization of the minimum domain required for targeting budding yeast myosin II to the site of cell division. *BMC Biol.* 4:19.
63. Margolin, W. 2005. FtsZ and the division of prokaryotic cells and organelles. *Nat. Rev. Mol. Cell Biol.* 6:862–871.
64. Dajkovic, A., and J. Lutkenhaus. 2006. Z ring as executor of bacterial cell division. *J. Mol. Microbiol. Biotechnol.* 11:140–151.
65. Lu, C., M. Reedy, and H. P. Erickson. 2000. Straight and curved conformations of FtsZ are regulated by GTP hydrolysis. *J. Bacteriol.* 182:164–170.
66. Erickson, H. P. 2001. The FtsZ protofilament and attachment of ZipA—structural constraints on the FtsZ power stroke. *Curr. Opin. Cell Biol.* 13:55–60.

67. Gilson, P. R., X. C. Yu, D. Hereld, C. Barth, A. Savage, B. R. Kiefel, S. Lay, P. R. Fisher, W. Margolin, and P. L. Beech. 2003. Two *Dictyostelium* orthologs of the prokaryotic cell division protein FtsZ localize to mitochondria and are required for the maintenance of normal mitochondrial morphology. *Eukaryot. Cell.* 2:1315–1326.

68. Thanedar, S., and W. Margolin. 2004. FtsZ exhibits rapid movement and oscillation waves in helix-like patterns in *Escherichia coli*. *Curr. Biol.* 14:1167–1173.

69. Ben-Yehuda, S., and R. Losick. 2002. Asymmetric cell division in *B. subtilis* involves a spiral-like intermediate of the cytokinetic protein FtsZ. *Cell.* 109:257–266.

70. Yeong, F. M. 2005. Severing all ties between mother and daughter: cell separation in budding yeast. *Mol. Microbiol.* 55:1325–1331.

71. Wolkow, T. D., S. D. Harris, and J. E. Hamer. 1996. Cytokinesis in *Aspergillus nidulans* is controlled by cell size, nuclear positioning and mitosis. *J. Cell Sci.* 109:2179–2188.

72. Chang, F. 2001. Studies in fission yeast on mechanisms of cell division site placement. *Cell Struct. Funct.* 26:539–544.

73. Burgess, D., and F. Chang. 2005. Site selection for the cleavage furrow at cytokinesis. *Trends Cell Biol.* 15:156–162.

74. O'Connell, C., A. Warner, and Y. Wang. 2001. Distinct roles of the equatorial and polar cortices in the cleavage of adherent cells. *Curr. Biol.* 11:702–707.

75. Uyeda, T., C. Kitayama, and S. Yumura. 2000. Myosin II independent cytokinesis in *Dictyostelium*: its mechanism and implications. *Cell Struct. Funct.* 25:1–10.

76. Veksler, A., and N. S. Gov. 2007. Phase transitions of the coupled membrane-cytoskeleton modify cellular shape. *Biophys. J.* 93:3798–3810.

77. Miyoshi, H., S. K. Satoh, E. Yamada, and Y. Hamaguchi. 2006. Temporal change in local forces and total force all over the surface of the sea urchin egg during cytokinesis. *Cell Motil. Cytoskeleton.* 63:208–221.